Measurement of nuclear excitation functions for proton induced reactions (E_p = ???–55 MeV) on natural Fe

Andrew S. Voyles,[1, *] Eric F. Matthews,[1] Jonathan T. Morrell,[1] M. Shamsuzzoha Basunia,[2] Lee A. Bernstein,[2, 1] Jonathan W. Engle,[3, †] Stephen A. Graves,[4] Amanda M. Lewis,[1] and Alexander Springer[5]

[1]*Department of Nuclear Engineering, University of California, Berkeley, Berkeley, CA 94720, USA*
[2]*Nuclear Science Division, Lawrence Berkeley National Laboratory, Berkeley, CA 94720, USA*
[3]*Department of Medical Physics, University of Wisconsin – Madison, Madison, WI 53705, USA*
[4]*Department of Radiation Oncology, University of Iowa, Iowa City, IA 52242, USA*
[5]*Fakultät für Physik, Karlsruhe Institute of Technology, 76131 Karlsruhe, Germany*
(Dated: July 19, 2018)

An article usually includes an abstract, a concise summary of the work covered at length in the main body of the article.

use the optional argument of the \item command to give the category of each item.

TODO LIST

I. INTRODUCTION

Blah blah blah

Novel applications are being explored for several radionuclides whose production methodologies are not established, but their production requires accurate, high-fidelity cross section data.

II. EXPERIMENTAL METHODS AND MATERIALS

The work described herein follows the methods utilized in our recent work and established by Graves *et al.* for monitor reaction characterization of beam energy and fluence in stacked target irradiations [1, 2]. Preliminary analysis was previously reported in the Master's thesis of one co-author, but the conclusive results of this work are described here [3].

ASV: Do we really need to cite Alex's thesis?

A. Stacked-target design

ASV: Update these energies, post-analysis

A pair of target stacks were constructed for this work, due to the large energy range desired to be spanned. One stack covers the 55–20 MeV range and the other covers 25–5 MeV, to minimize the systematic uncertainties associated with degradation of beam energy. In addition, the complementary energy of the stacks helps build confidence through multiple overlapping measurements between 20–25 MeV. A series of nominal 25 µm ^{nat}Fe foils (99.5%), 25 µm ^{nat}Ti foils (99.6%), and 25 µm ^{nat}Cu foils (99.95%) were used (all from Goodfellow Corporation, Coraopolis, PA 15108, USA) targets were used. In each stack, seven foils of each metal were cut down to 2.5×2.5 cm squares and characterized — for each foil, length and width measurements were taken at four different locations using a digital caliper (Mitutoyo America Corp.), thickness measurements were taken at four different locations using a digital micrometer (Mitutoyo America Corp.), and four mass measurements were taken using an analytical balance after cleaning the foils with

---

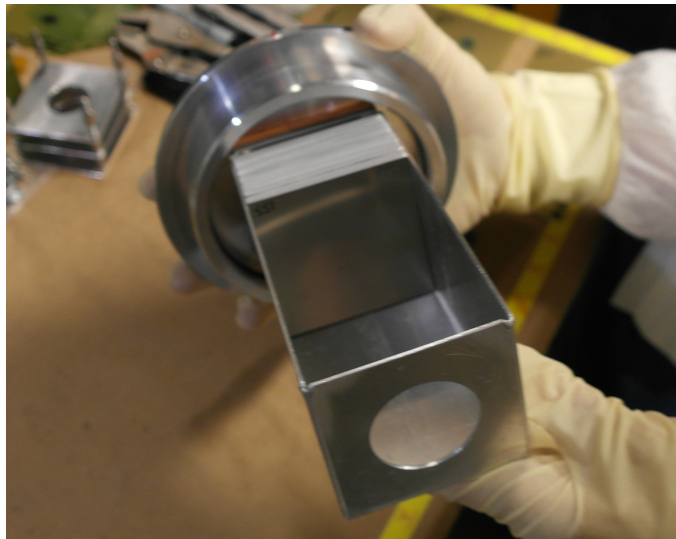* andrew.voyles@berkeley.edu
† jwengle@wisc.edu

Figure 1: Photograph of the assembled 25 MeV target stack, before it was mounted in the beamline. The proton beam enters through the circular entrance in the foreground, and the upstream stainless steel profile monitor is visible at the front of the stack.

isopropyl alcohol. Using these length, width, and mass readings, the areal density and its uncertainty (in mg/cm^2) for each foil was calculated. The foils were tightly sealed into "packets" using two pieces of 3M 1205-Series Kapton polyimide film tape — each piece of tape consists of 38.1 µm of an acrylic adhesive (nominal 4.49 mg/cm^2) on 25.4 µm of a polyimide backing (nominal 3.61 mg/cm^2). The sealed foils were mounted over the hollow center of a 1.5875 mm-thick aluminum frame. Targets of 6061 aluminum alloy serve as proton energy degraders between energy positions. The target box, seen in Figure 1, is machined from 6061 aluminum alloy, and mounts on the end of an electrically-isolated beamline. The specifications of both target stack designs for this work are presented in Table I.

Both target stacks were assembled and separately irradiated at the Lawrence Berkeley National Laboratory (LBNL), using the 88-Inch Cyclotron, a K=140 sector-focused cyclotron. The 25 MeV stack was irradiated for approximately 20 minutes with a nominal current of 100 nA, for an anticipated integral current of 31.61 nAh. The 55 MeV stack was irradiated for approximately 10 minutes with a nominal current of 120 nA, for an anticipated integral current of 20.78 nAh. The beam current, measured using a current integrator on the electrically-isolated beamline, remained stable under these conditions for the duration of each irradiation. The proton beam incident upon each stack's upstream stainless steel profile monitor had a maximum energy of either 25 or 55 MeV, with an approximately 2% energy width due to multi-turn extraction — these energy profiles were used for all later analysis. Following end-of-bombardment (EoB), each stack was removed from the beamline and disassembled. All activated foils were transported to a counting lab for gamma spectrometry, which started approximately 30 minutes following the end of each irradiation.

B. Quantification of induced activities

A single detector was used in this measurement, an ORTEC GMX Series (model #GMX-50220-S) High-Purity Germanium (HPGe) detector. The detector is a nitrogen-cooled coaxial n-type HPGe with a 0.5 mm beryllium window, and a 64.9 mm diameter, 57.8 mm long crystal. Samples were counted at fixed positions ranging 5–60 cm (5% maximum permissible dead-time) from the front face of the detector, with a series of standard calibration sources used to determine energy and efficiency for each position. The foils were counted for a period of 4 weeks following end-of-bombardment (EoB), to accurately quantify all induced activities. An example of one of the gamma-ray spectra collected in such a fashion is shown in Figure 2. For all spectra collected, net peak areas were fitted using the gamma spectrometry analysis code FitzPeaks [4], which utilizes the SAMPO fitting algorithms for gamma ray spectra [5].

The net counts in each fitted gamma-ray photopeak were converted into activities for the decaying activation products, using calibrated detector efficiencies and gamma-ray intensities for each transition. The nuclear decay data used in this work is tabulated, for reference, in Table II and Table III of Appendix A. Corrections for gamma-ray attenuation within each foil packet were made, using photon attenuation coefficients from the XCOM photon cross sections database [6]. The total propagated uncertainty in activity is the quadrature sum of the uncertainty in fitted peak areas, uncertainty in detector efficiency calibration, and uncertainty in the gamma-ray branching ratio data.

Table I: Specifications of the 25 MeV and 55 MeV target stack designs in the present work. The proton beam enters the stack upstream of the SS-5 and SS-3 profile monitors, respectively, and is transported through the stack in the order presented here. The 6061 aluminum degraders have a measured density of approximately 2.69 g/cm^3. Their areal densities were determined using the variance minimization techniques described in this work and our earlier paper [1]. A 316 stainless steel foil is inserted at both the front and rear of each target stack as a monitor of the beam's spatial profile, by developing radiochromic film (Gafchromic EBT3) after end-of-bombardment (EoB).

25 MeV Target layer	Measured thickness	Measured areal density (mg/cm^2)	Uncertainty in areal density (%)	55 MeV Target layer	Measured thickness	Measured areal density (mg/cm^2)	Uncertainty in areal density (%)
SS profile monitor SS-5	130.94 µm	100.57	0.17	SS profile monitor SS-3	130.9 µm	100.48	0.17
Fe-08	26.25 µm	19.69	0.17	Fe-01	25.75 µm	20.22	0.21
Ti-14	25.01 µm	10.87	0.36	Ti-01	25.88 µm	11.09	0.16
Cu-14	24.01 µm	17.49	0.40	Cu-01	28.81 µm	22.40	0.11
Al Degrader E-09	256.5 µm	–	–	Al Degrader A-1	2.24 mm	–	–
Fe-09	26.5 µm	19.90	0.09	Fe-02	25.5 µm	19.91	0.13
Ti-15	23.81 µm	10.97	0.11	Ti-02	25.74 µm	10.94	0.24
Cu-15	21.81 µm	17.63	0.46	Cu-02	28.75 µm	22.32	0.40
Al Degrader H-01	127.09 µm	–	–	Al Degrader A-2	2.24 mm	–	–
Fe-10	26.5 µm	19.84	0.11	Fe-03	25.25 µm	20.00	0.27
Ti-16	24.6 µm	10.96	0.32	Ti-03	25.91 µm	11.25	0.15
Cu-16	22.01 µm	17.22	0.25	Cu-03	28.86 µm	22.49	0.20
Fe-11	27.26 µm	19.96	0.17	Al Degrader C-1	0.97 mm	–	–
Ti-17	25.01 µm	10.88	0.25	Fe-04	25.25 µm	19.93	0.33
Cu-17	29 µm	21.91	0.33	Ti-04	25.84 µm	10.91	0.18
Fe-12	27.01 µm	20.03	0.12	Cu-04	28.78 µm	22.38	0.29
Ti-18	25.01 µm	11.00	0.87	Al Degrader C-2	0.97 mm	–	–
Cu-18	28.75 µm	22.33	0.14	Fe-05	25.64 µm	20.02	0.24
Fe-13	26.25 µm	20.05	0.16	Ti-05	25.86 µm	10.99	0.30
Ti-19	26.6 µm	11.01	0.22	Cu-05	28.77 µm	22.35	0.12
Cu-19	28.75 µm	22.32	0.19	Al Degrader C-3	0.97 mm	–	–
Fe-14	25.75 µm	20.11	0.19	Fe-06	25.75 µm	20.21	0.26
Ti-20	27.01 µm	11.06	0.35	Ti-06	25.5 µm	11.15	0.23
Cu-20	28.26 µm	22.34	0.28	Cu-06	28.83 µm	22.43	0.10
SS profile monitor SS-6	131.5 µm	100.99	0.17	Al Degrader C-4	0.97 mm	–	–
				Fe-07	25.76 µm	19.93	0.19
				Ti-07	25.75 µm	11.17	0.33
				Cu-07	28.76 µm	22.34	0.24
				Al Degrader H-02	127.04 µm	–	–
				SS profile monitor SS-4	131.21 µm	101.25	0.16

As in our previous work, these activities used to calculate cross sections, and are differentiated between cumulative and independent [1]. For the first observable product nuclei in a mass chain, its (p,x) cross section will be reported as a cumulative cross section (σ_c), which is the sum of direct production of that nucleus, as well as decay of its precursors and any other independent cross sections leading to that nucleus. Cumulative cross sections will be reported whenever it is impossible to use decay spectrometry to distinguish independent production of a nucleus from decay feeding. For all remaining observed reaction products in the mass chain, and cases where no decay precursors exist, independent cross sections (σ_i) will be reported, allowing for determination of the independent production via subtraction and facilitating comparison to reaction model calculations. Solutions to the first- and higher-order Bateman equations are used for separation of feeding contributions from decay precursors, that independent cross sections may be reported [7, 8].

C. Proton fluence determination

In addition to the stack's overall beam current measurements using beamline current integrators, thin ^{nat}Ti and ^{nat}Cu foils were included along with the ^{nat}Fe targets at each energy position, to monitor beam current at each position within the stack. The IAEA-recommended ^{nat}Ti(p,x)^{46}Sc, ^{nat}Ti(p,x)^{48}V, ^{nat}Cu(p,x)^{62}Zn, and ^{nat}Cu(p,x)^{63}Zn monitor reactions were used for proton fluence measurement [9]. As in our previous work, the integral form of the well-known
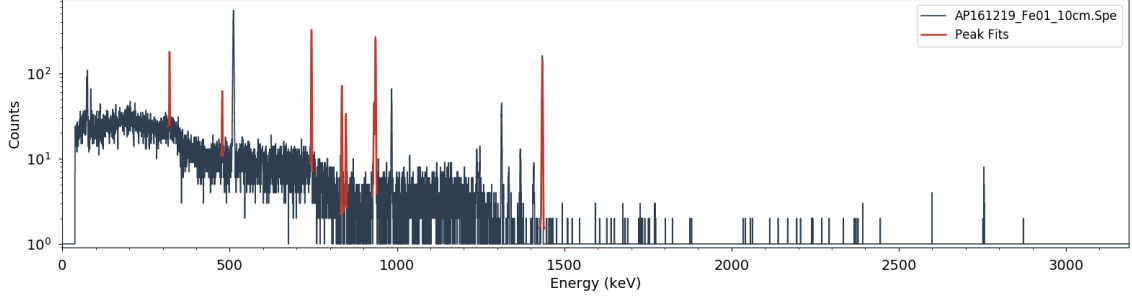
Figure 2: Replace this figure!!! A gamma spectrum collected from an activated Fe foil at approximately 80 MeV. While the majority of observed reaction products are visible in this spectrum, the ^{51}Cr, ^{52m}Mn, and ^{52g}Mn decay lines, which form the primary reaction channels of interest, are clearly isolated from surrounding peaks.

activation equation was used to determine proton fluence ($I\Delta t$), in order to account for energy loss across each monitor foil:

$$I\Delta t = \frac{A_0 \Delta t}{\rho \Delta r \left(1 - e^{-\lambda \Delta t}\right) \int \sigma\left(E\right) \frac{d\phi}{dE} dE} \tag{1}$$

The propagated uncertainty in proton fluence is calculated as the quadrature sum of (1) the uncertainty in quantified EoB activity, (2) uncertainty in the duration of irradiation (conservatively estimated at 60 s, to account for any transient changes in beam current), (3) uncertainty in foil areal density, (4) uncertainty in monitor product half-life (included, but normally negligible), (5) uncertainty in IAEA recommended cross section (using values from the 2017 IAEA re-evaluation [9]), and (6) uncertainty in differential proton fluence (from transport simulations).

D. Proton transport calculations

Estimates of the proton beam energy for preliminary stack designs were calculated using the Anderson & Ziegler (A&Z) stopping power formalism [10–12]. However, the more rigorous Monte Carlo N-Particle transport code MCNP6.1 was used for simulation of the full 3-D target stack, to determine the full proton energy and fluence distribution for each foil [13]. 10^8 source protons were used for all MCNP simulations, which places the statistical uncertainty in proton energy distributions at less than 0.01%. As with the determination of proton fluence in monitor foils, the progressively increasing energy straggle towards the rear of each stack is accounted for using the differential proton fluence from MCNP simulation of proton transport. These energy distributions $\frac{d\phi}{dE}$ are used to calculate a flux-weighted average proton energy $\langle E \rangle$, which accounts for the slowing-down of protons within a foil (particularly in the low-energy stack) and reports the effective energy centroid for each foil:

$$\langle E \rangle = \frac{\int E \frac{d\phi}{dE} dE}{\int \frac{d\phi}{dE} dE} \tag{2}$$

To report a complete description of the representative energy for each foil, a bin width is provided through the energy uncertainty, calculated as the full width at half maximum (FWHM) of the MCNP6-modeled energy distribution for each foil.

To correct for a spread in the apparent proton fluence, seen most strongly in rear stack positions, the "variance minimization" techniques utilized in our recent work and established by Graves *et al.* have been used to reduce uncertainty in proton fluence assignments [1, 2]. This method is based on the assumption that the independent measurements of proton fluence from the different monitor reactions used in this work should all be consistent at each energy position. Assuming that the recommended monitor reaction cross sections and MCNP6-modeled energy distributions are both accurate, residual disagreement in the observed proton fluences is thus primarily due to poorly characterized stopping power in simulations, or a systematic error in the areal densities of the stack components. This disagreement is minor at the front of the stack, and gets progressively worse as the beam is degraded, due to the compounded effect of systematic uncertainties in stack areal densities.

When performing a variance minimization, it is important to apply this variation of effective areal density to the stack components which have the most significant impact on beam degradation, as any systematic error in the areal densities used for these components will cause a disagreement in the observed fluences. For the 55 MeV stack, the aluminum degraders are used for variance minimization, as they make up more than 80% of the areal density of the stack, and this play the largest role in beam degradation.

Update this post-results! For the 25 MeV stack, the Kapton tape was chosen for variance minimization, as the foil packets themselves are responsible for the majority of beam degradation. While it only makes up approximately 20% of the low-energy stack's areal density, the Kapton surrounding each foil packet has a greater areal density than the foil itself. In addition, it is far easier to directly characterize the areal density of the metallic foils than it is for the Kapton, resulting in only an approximate value for the latter. This is of relatively minor consequence for higher-energy irradiations (especially relative to any beam degraders), but the stopping power of the Kapton at this energy range may cause as much as a loss of 0.5 MeV by the rear of this stack, making the precise areal density a source of significant uncertainty.

In performing the minimization, the areal density of each of the aluminum degraders (for the 55 MeV stack) were varied uniformly in MCNP6 simulations by a factor of up to $\pm 25\%$ of nominal values, to find the effective density which minimized variance in the measured proton fluence at the lowest energy position (Ti-07, Cu-07). For the 25 MeV stack, the areal density of the E-09 and H-01 aluminum degraders was taken from that reached in the minimization of the 55 MeV stack. Using this value, the areal density of each of the Kapton tape layers were likewise varied uniformly by a factor of up to $\pm 25\%$ of nominal values, to find the effective density which minimized variance in the measured proton fluence at the next-to-lowest energy position (Ti-19, Cu-19). These lowest energy positions were chosen as minimization candidates, as they are the most sensitive to systematic uncertainties in stack design, due to the compounded effect of proton stopping powers. In the 25 MeV stack, activity was not seen in gamma spectrometry for the lowest-energy (Ti-20, Cu-20) monitor foils, implying that the beam was stopped at some point in between Fe-14 and Ti-20. This observation is conclusive proof that the true areal densities of the stack components differs from nominally measured values (primarily for the difficult-to-characterize Kapton tape), as transport calculations using nominal areal densities predict that the beam should exit the stack (at the SS-6 profile monitor) with an energy of approximately 7 MeV. As a result, this position was not used for minimization, with the Ti-19 and Cu-19 position being the lowest-energy reliable monitor foils in the stack. The results of the minimization technique indicate a clear minimum in proton fluence variance for flux-weighted average 41.34 MeV protons entering the last energy position of the 55 MeV stack. This is approximately 2 MeV lower than the nominal MCNP6 simulations, and approximately 3 MeV lower than nominal A&Z calculations, both of which used the nominal 2.80 g/cm^3 measured density of the aluminum degraders. This energy corresponds to an aluminum areal density of 2.52% greater than nominal measurements, and serves as a lump correction for other minor systematic uncertainties in stack design, including stack areal densities and incident beam energy. Similarly, for the 25 Me stack, variance minimization converges on flux-weighted average 41.34 MeV protons entering the Fe-13/Ti-19/Cu-19 energy position, which is approximately 2 MeV lower than the nominal MCNP6 simulations, and approximately 3 MeV lower than nominal A&Z calculations. This energy corresponds to a Kapton tape areal density of 2.52% greater than nominal measurements. The impact of this variance minimization for improving disagreement in proton fluence is clearly seen in Figure 3.

An enhanced version of the final ^{nat}Ti(p,x)^{46}Sc, ^{nat}Ti(p,x)^{48}V, ^{nat}Cu(p,x)^{62}Zn, and ^{nat}Cu(p,x)^{63}Zn monitor reaction fluences is shown in Figure 4. The uncertainty-weighted mean for the two ^{nat}Cu(p,x) and two ^{nat}Ti(p,x) monitor channels was calculated at each energy position, to determine the final fluence assignments for the Cu and Ti foils, respectively, and the uncertainty-weighted mean for all four monitor channels was used to determine the final fluence assignments for the Fe foils. Uncertainty in proton fluence is calculated by error propagation of the fluence values at each energy position. These weighted-mean fluences are plotted in Figure 4, along with the estimated fluence according to both MCNP6 transport and an uncertainty-weighted linear χ^2 fit to the individual monitor channel fluence measurements. Both models reproduce the observed fluence data consistently within uncertainty, with the MCNP6 model predicting a slightly greater fluence loss throughout the stack. These models are used purely to provide an extrapolation from the highest-energy position back to the "front" of each stack, to compare with the nominal fluence measured by the beamline current integrators.

E.   Calculation of measured cross sections

Using the quantified EoB activities along with the variance-minimized proton fluence, it is possible to calculate the final cross sections for the various observed (p,x) reactions. While thin ($\approx$ 10–20 mg/cm^2) foils were irradiated to minimize the energy bins of these cross section measurements, it is important to note that all cross sections reported here are flux-averaged over the energy distribution subtended by each foil, as seen in Figure 5. For both the cumulative
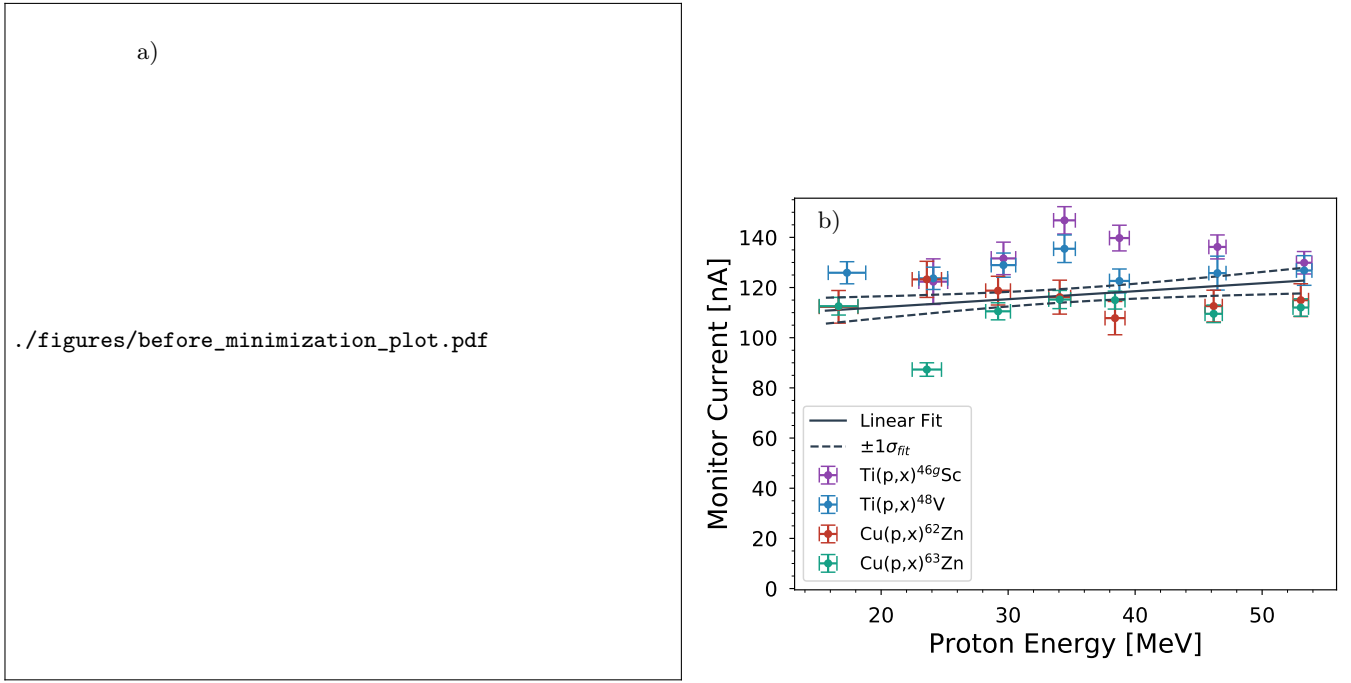
Figure 3: Update this figure!!! Results of variance minimization through enhancement of the effective areal density of the aluminum degraders by 2.52% (55 MeV stack) and Kapton tape by 2.52% (25 MeV stack). A noticeable reduction of variance in measured proton fluence is seen, particularly at the rear stack positions.
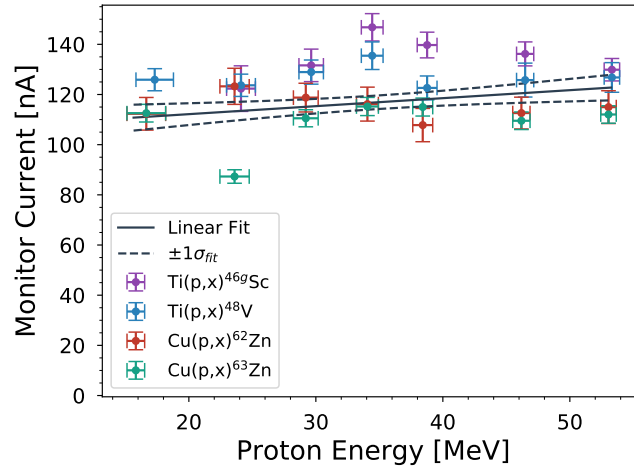

Figure 4: Update this figure!!! Final uncertainty-weighted mean proton fluences throughout the target stack, based on the variance-minimized observed fluence from the the ^{nat}Ti(p,x)^{46}Sc, ^{nat}Ti(p,x)^{48}V, ^{nat}Cu(p,x)^{62}Zn, and ^{nat}Cu(p,x)^{63}Zn monitor reactions. The fluence drops by approximately 7.2–8.9% from the incident fluence of 196.9–198.8 nAh over the length of the target stack, based on fluence loss models from MCNP6 simulations and an empirical fit to fluence measurements.

and independent activities quantified, cross sections were calculated as:

$$\sigma = \frac{A_0}{\rho \Delta r I \left(1 - e^{-\lambda \Delta t}\right)} \quad (3)$$

where A_0 is the EoB activity for the monitor reaction product, I is the proton current, $\rho \Delta r$ is the foil's areal density, λ is the monitor reaction product's decay constant, and Δt is the length of irradiation. The beam current, measured
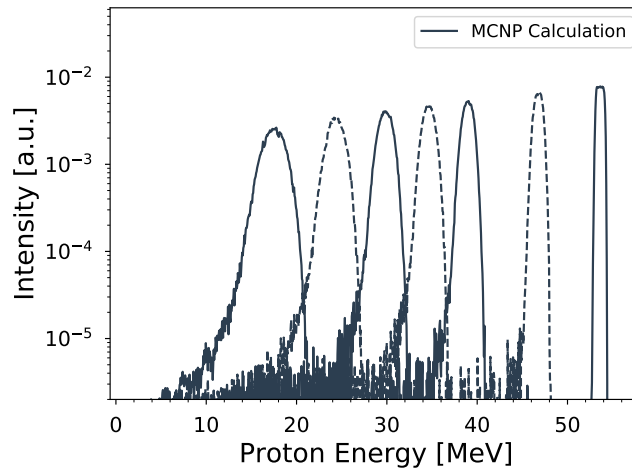
Figure 5: Add 25 MeV stack tallies here! Final variance minimized incident proton energy distributions for the Fe foils, as simulated in MCNP6. The distribution tallies in each foil are all normalized to be per source proton, which was 10^8 in all simulations. As the beam is degraded, proton energy distributions become visibly broadened due to straggling, and drop in magnitude due to scattering losses.

using a current integrator connected to the electrically-isolated target box, remained stable for the duration of the irradiation. The propagated uncertainty in cross section is calculated as the quadrature sum of the uncertainty in quantified EoB activity (which includes uncertainty in detector efficiencies), uncertainty in the duration of irradiation (conservatively estimated at 30 s, to account for any minor transient changes in beam current), uncertainty in foil areal density, uncertainty in monitor product half-life (included, but normally negligible), and uncertainty in proton current (quantified by error propagation of the monitor reaction fluence values at each energy position, as seen in Figure 4).

III. RESULTS AND DISCUSSION

Blah blah blah

IV. CONCLUSIONS

Blah blah blah

V. ACKNOWLEDGEMENTS

Appendix A: Decay data

The lifetimes and gamma-ray branching ratios listed in these tables were used for all calculations of measured cross sections reported in this work, and have been taken from the most recent edition of Nuclear Data Sheets for each mass chain

Table II: Decay data for gamma-rays observed in $^{\mathrm{nat}}$Ti(p,x) and $^{\mathrm{nat}}$Cu(p,x).

Nuclide	Half-life	E_γ (keV)	I_γ (%)
^{22}Na	2.6018(22) y	1274.537	99.940(14)

Table III: Decay data for gamma-rays observed in $^{\mathrm{nat}}$Fe(p,x).

Nuclide	Half-life	E_γ (keV)	I_γ (%)
^{82m}Rb	6.472(6) h	554.35	62.4(9)
	6.472(6) h	619.11	37.98(9)

Appendix B: Measured excitation functions

Figures of the cross sections measured in this work are presented here, in comparison with literature data

Appendix C: Measured isomer-to-ground state branching ratios

Plots of the isomer-to-ground state ratios measured in this work are presented here, in comparison with literature data and reaction modeling codes

[1] A. S. Voyles, L. A. Bernstein, E. R. Birnbaum, J. W. Engle, S. A. Graves, T. Kawano, A. M. Lewis, and F. M. Nortier, Nuclear Instruments and Methods in Physics Research Section B: Beam Interactions with Materials and Atoms **429**, 53 (2018).
[2] S. A. Graves, P. A. Ellison, T. E. Barnhart, H. F. Valdovinos, E. R. Birnbaum, F. M. Nortier, R. J. Nickles, and J. W. Engle, Nuclear Instruments and Methods in Physics Research, Section B: Beam Interactions with Materials and Atoms **386**, 44 (2016).
[3] A. Springer, (2017), arXiv:1707.05908.
[4] J. Fitzgerald, "FitzPeaks gamma analysis and calibration software," (2009).
[5] P. A. Aarnio, M. T. Nikkinen, and J. T. Routti, Journal of Radioanalytical and Nuclear Chemistry **248**, 371 (2001).
[6] M. J. Berger, J. H. Hubbell, S. M. Seltzer, J. Chang, J. S. Coursey, R. Sukumar, D. S. Zucker, and K. Olsen, (2010).
[7] H. Bateman, in *Proc. Cambridge Philos. Soc*, Vol. 15 (1910) pp. 423–427.
[8] J. Cetnar, Annals of Nuclear Energy **33**, 640 (2006).
[9] A. Hermanne, A. Ignatyuk, R. Capote, B. Carlson, J. Engle, M. Kellett, T. Kibédi, G. Kim, F. Kondev, M. Hussain, O. Lebeda, A. Luca, Y. Nagai, H. Naik, A. Nichols, F. Nortier, S. Suryanarayana, S. Takács, F. Tárkányi, and M. Verpelli, Nuclear Data Sheets **148**, 338 (2018).
[10] H. H. Andersen and J. F. Ziegler, *Hydrogen stopping powers and ranges in all elements* (Pergamon Press,New York, 1977).
[11] J. F. Ziegler and J. P. Biersack, "The Stopping and Range of Ions in Matter," in *Treatise on Heavy-Ion Science: Volume 6: Astrophysics, Chemistry, and Condensed Matter*, edited by D. A. Bromley (Springer US, Boston, MA, 1985) pp. 93–129.
[12] J. F. Ziegler, Journal of Applied Physics **85**, 1249 (1999).
[13] T. Goorley, M. James, T. Booth, F. Brown, J. Bull, L. J. Cox, J. Durkee, J. Elson, M. Fensin, R. A. Forster, J. Hendricks, H. G. Hughes, R. Johns, B. Kiedrowski, R. Martz, S. Mashnik, G. McKinney, D. Pelowitz, R. Prael, J. Sweezy, L. Waters, T. Wilcox, and T. Zukaitis, Nuclear Technology **180**, 298 (2012).